Perovskite Cathodes for Aqueous and Organic Iodine Batteries Operating Under One and Two Electrons Redox Modes

Li, Xinliang; Wang, Shixun; Zhang, Dechao; Li, Pei; Chen, Ze; Chen, Ao; Huang, Zhaodong; Liang, Guojin; Rogach, Andrey L.; Zhi, Chunyi

Published in:
Advanced Materials

Published: 25/01/2024

Document Version:
Post-print, also known as Accepted Author Manuscript, Peer-reviewed or Author Final version

Published version (DOI):
10.1002/adma.202304557

Publication details:
Li, X., Wang, S., Zhang, D., Li, P., Chen, Z., Chen, A., Huang, Z., Liang, G., Rogach, A. L., & Zhi, C. (2024). Perovskite Cathodes for Aqueous and Organic Iodine Batteries Operating Under One and Two Electrons Redox Modes. *Advanced Materials*, *36*(4), Article 2304557. https://doi.org/10.1002/adma.202304557

Perovskite cathodes for aqueous and organic iodine batteries operating under one and two electrons redox modes

Xinliang Li[1#], Shixun Wang[2,3#], Dechao Zhang[2], Pei Li[2], Ze Chen[2], Ao Chen[2], Zhaodong Huang[2,4], Guojin Liang[2], Andrey L. Rogach[2,3], Chunyi Zhi[2,3,4*]*

[1]Key Laboratory of Material Physics, Ministry of Education, School of Physics and Microelectronics, Zhengzhou University, Zhengzhou, 450052, China

[2]Department of Materials Science and Engineering, City University of Hong Kong, 83 Tat Chee Avenue, Hong Kong S.A.R., 999077, China

[3]Center for Functional Photonics, City University of Hong Kong, 83 Tat Chee Avenue, Hong Kong S.A.R., 999077, China

[4]Hong Kong Center for Cerebro-Cardiovascular Health Engineering (COCHE), Shatin, NT, Hong Kong S.A.R., 999077, China

*Corresponding authors. E-mail: andrey.rogach@cityu.edu.hk (ALR); cy.zhi@cityu.edu.hk (CZ)

[#]X.L. and S.W. contributed equally to this work

Abstract

Although conversion-type iodine-based batteries are considered promising for energy storage systems, stable electrode materials are scarce, especially for high-performance multi-electron reactions. We suggest using tin-based iodine-rich two-dimensional (2D) Dion–Jacobson (DJ)

This article has been accepted for publication and undergone full peer review but has not been through the copyediting, typesetting, pagination and proofreading process, which may lead to differences between this version and the Version of Record. Please cite this article as doi: 10.1002/adma.202304557.

$ODASnI_4$ (ODA: 1,8-octanediamine) perovskite materials as cathode materials for iodine-based batteries. As a proof of concept, organic lithium-perovskite and aqueous zinc-perovskite batteries are fabricated and they can be operated based on the conventional one-electron and advanced two-electron transfer modes. The active elemental iodine in the perovskite cathode provides capacity through a reversible I^-/I^+ redox pair conversion at full depth, and the rapid electron injection/extraction leads to excellent reaction kinetics. Consequently, high discharge plateaus (1.71 V versus Zn^{2+}/Zn; 3.41 V versus Li^+/Li), large capacity (421 mAh g^{-1}_I), and a low decay rate (1.74 mV/mAh g^{-1}_I) are achieved for lithium and zinc ion batteries, respectively. This study demonstrates the promising potential of perovskite materials for high-performance metal-iodine batteries. Their reactions based on the two-electron transfer mechanism shed light on similar battery systems aiming for decent operational stability and high energy density.

Keywords: Dion–Jacobson tin-iodide perovskite, perovskite cathode, active iodine ligand, multi-electron reaction, conversion-type batteries

1. Introduction

Advances in electronic technology are fuelling increased demand for energy storage devices.[1] The conversion-type batteries have gradually exhibited advantages over conventional rocking-chair rivals.[2] They are considered one of the most promising candidates for next-generation energy storage systems, with cost-effective and large capacity attributes, and are attracting increasing interest.[3] As a typical representative, iodine-based battery is suitable for aqueous and organic electrolytes and holds the benefits of flat discharge voltage plateaus and high energy density.[4]

The following challenges must be overcome before iodine-based batteries can be widely applied in practical settings. First, electrochemically active substances that contain iodine are scarce.[5] Iodine itself also has several intrinsic drawbacks. It is insulating and volatile and relies on a large amount of porous conductive host to transport electrons, resulting in a low

volume of electrochemically active content and a short shelf life.[6] Without a highly effective host, the I_2 loss is extensive, and the redox kinetics are hysteretic.[7] Second, the universality of the multi-electron conversion mechanism and adaptive electrolytes in both aqueous and organic batteries has not yet been demonstrated.[8] Two-electron conversion of an elemental iodine electrode in the highly concentrated acetonitrile-containing electrolyte was achieved in a recent study and found to boost electrochemical performance.[4a] At the same time, this approach fundamentally sacrifices the intrinsic safety and applicability of aqueous batteries.[9] Novel iodine electrodes that undergo two-electron transfer in various electrolytes should be developed.

Metal halide perovskite materials, with the general chemical formula AMX_3 (*A*: monovalent cation; *M*: divalent metal cation; *X*: halogen), consist of organic or inorganic cations and halogen anions.[10] Such metal halide perovskites exhibit excellent photovoltaic performance and have, over the last decade, become the most sought-after solar cell component.[11] Low-dimensional lead-free perovskite materials have been developed to address toxicity concerns of the commonly employed lead-based perovskites and to optimize internal electron transport pathways and mobility with their adjusted lattice relaxation.[12] The type, combination, and number of coordinated halogen ions in these materials can be tailored by tweaking the raw materials and synthesis technique to meet diverse requirements for crystal and electronic structures and halogen content.[13] Interestingly, studies on failure mechanisms of perovskites in solar cells demonstrated that halogen anions could be oxidized by photo-generated holes, suggesting that the binding energy of halogens in perovskites is limited and providing an opportunity to activate them for electrochemical energy storage.[14]

In this study, we employed two-dimensional (2D) Dion–Jacobson (DJ) tin-based iodine-rich perovskite microcrystals with a structural formula $ODASnI_4$ (ODA: 1,8-octanediamine) as cathodes in both aqueous Zn ion and organic Li ion batteries. As an alternative to conventional I_2, 2D $ODASnI_4$ perovskite ensures high iodine content (more than 65%) while circumventing its long-criticized physicochemical instability. When serving

as the cathode in aqueous Zn ion and organic Li ion batteries, it fully applies to one-electron and two-electron redox modes through a solid-liquid transition. It has exceptional reaction kinetics and sufficient transition depth. The *in-situ* Raman, *ex-situ* X-ray photoelectron spectroscopy (XPS), and DFT simulation revealed that the charge storage mechanism of the developed halide perovskite electrode solely depends on the reversible redox conversion of iodine.

2. Results and discussions

As demonstrated in **Figure 1a**, corner-sharing $[SnI_6]^{4-}$ octahedra formed 2D inorganic slabs comprising $ODASnI_4$ microcrystals with octane-1,8-diammonium cations. Scanning electron microscopy (SEM) results confirmed the 2D appearance of the $ODASnI_4$ microcrystals (**Figure 1b**). The presence of N, Sn, and I elements were revealed by energy-dispersive X-ray spectroscopy (EDS), showing an atomic ratio close to 1:4 (Sn: I) (**Figure S1**). X-ray photoelectron spectroscopy (XPS) measurement was subsequently conducted, revealing the Sn:I atomic ratio of approximately 1: 4, similar to that obtained through EDS (**Figures 1c** and **S2**). Two peaks located at 619.1 and 630.5 eV were attributed to I^-. As evidenced by the X-ray diffraction (XRD) pattern shown in **Figure 1d**, the synthesized $ODASnI_4$ microcrystals presented a strong crystallization peak at a low degree of diffraction (6.6°), which is the typical feature of low-dimensional perovskites.[10b] XRD simulation was further conducted and showed that $ODASnI_4$ consisted of an alternating coordinated organic layer and inorganic lead iodide slab that corresponded to ODA^{2+} cations and corner-sharing $[SnI_6]^{4-}$ octahedra. It demonstrated a highly preferred growth orientation along the (002) lattice plan, which promoted the formation of 2D DJ-phase $ODASnI_4$. The Fourier transform infrared (FT-IR) spectrum in **Figure 1e** confirmed the existence of N–H stretching and bending vibrations at 3421 and 1621 cm^{-1}, respectively, due to the protonation of primary amine groups of ODA chains that bounded with the inorganic slabs in the form of N-H…I hydrogen bonds.[15] Notably, the thermogravimetric analysis (TGA) indicated superior thermal stability of $ODASnI_4$ microcrystals to I_2 (**Figure S3**). The temperature at

which the weight dropped sharply was over 200 °C for $ODASnI_4$ microcrystals and only about 60 °C for I_2. The identified superior thermal stability will facilitate preparation processes and optimize the shelf life of $ODASnI_4$ electrodes.

The electrochemical properties of the perovskite cathodes (PSC) based on $ODASnI_4$ microcrystals were subsequently measured. Zn metal and $ZnSO_4$ solution were employed as the anode and electrolyte in an aqueous Zn battery. Li metal and an ether electrolyte (LiTFSI + $LiNO_3$ in dimethoxyethane + 1,3-dioxolane) were used in a lithium-ion battery. In the subsequent discussion, aqueous Zn||PSC and organic Li||PSC batteries are referred to as AZP and OLP, respectively.

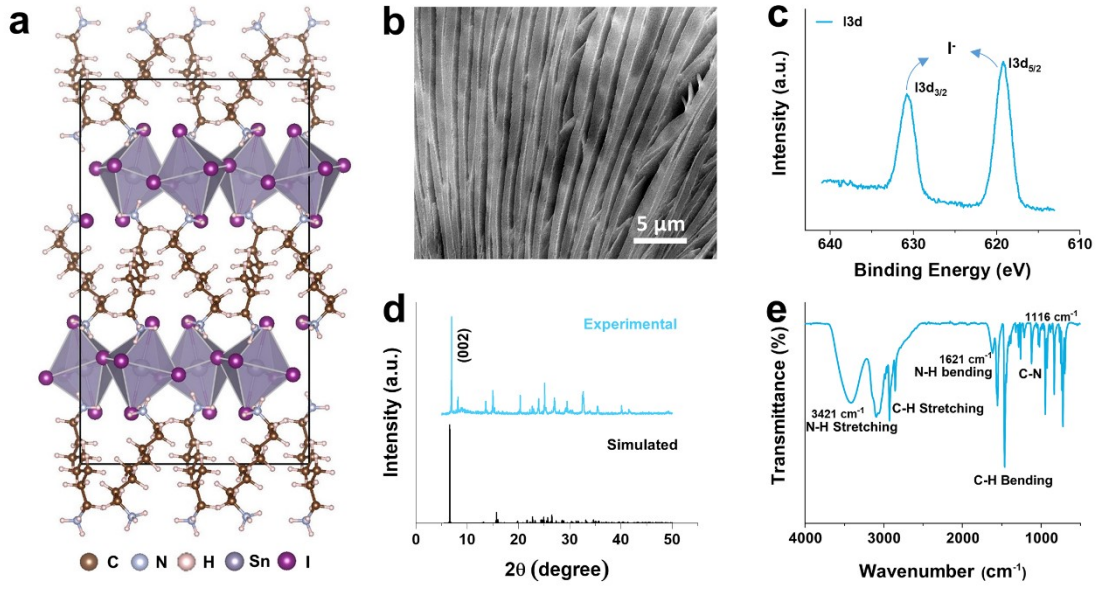

Figure 1. Characterization of 2D $ODASnI_4$ perovskite microcrystals. a) Schematic diagram. b) SEM image. c) High-resolution I3d XPS spectrum. d) Experimental and simulated XRD patterns of $ODASnI_4$. e) FT-IR spectrum.

As shown in **Figure 2a**, at a sweep rate of 0.5 mV s^{-1}, the cyclic voltammetry (CV) curves contain a pair of distinct redox peaks in both cases, which appear at 1.10/1.25 V versus Zn^{2+}/Zn for the AZP and 2.90/3.00 V versus Li^{+}/Li for the OLP, corresponding to the

one-electron redox mechanism of the I⁻ anion, similar to that of the conventional I_2 cathode.[16] Four key features of the CV curves corroborate the electrochemical benefits of the PSC and warrant highlighting. First, no other electrochemical signal was revealed apart from the I⁻ redox signal, suggesting that a single-step conversion directly drove the entire reaction.[17] Second, excellent reaction kinetics were evidenced by the sharp redox peaks with narrow half-peak widths.[18] Third, the superior symmetry of the current response implied superior reversibility.[19] Fourth, almost all of the charge storage was contributed exclusively by I⁻ redox conversion because the peak area essentially covered the entire CV curve.[20] These observations point out that the iodine source in the PSC has exceptional electrochemical activity and redox kinetics, to which its specific electron injection/extraction mechanism may have contribution.

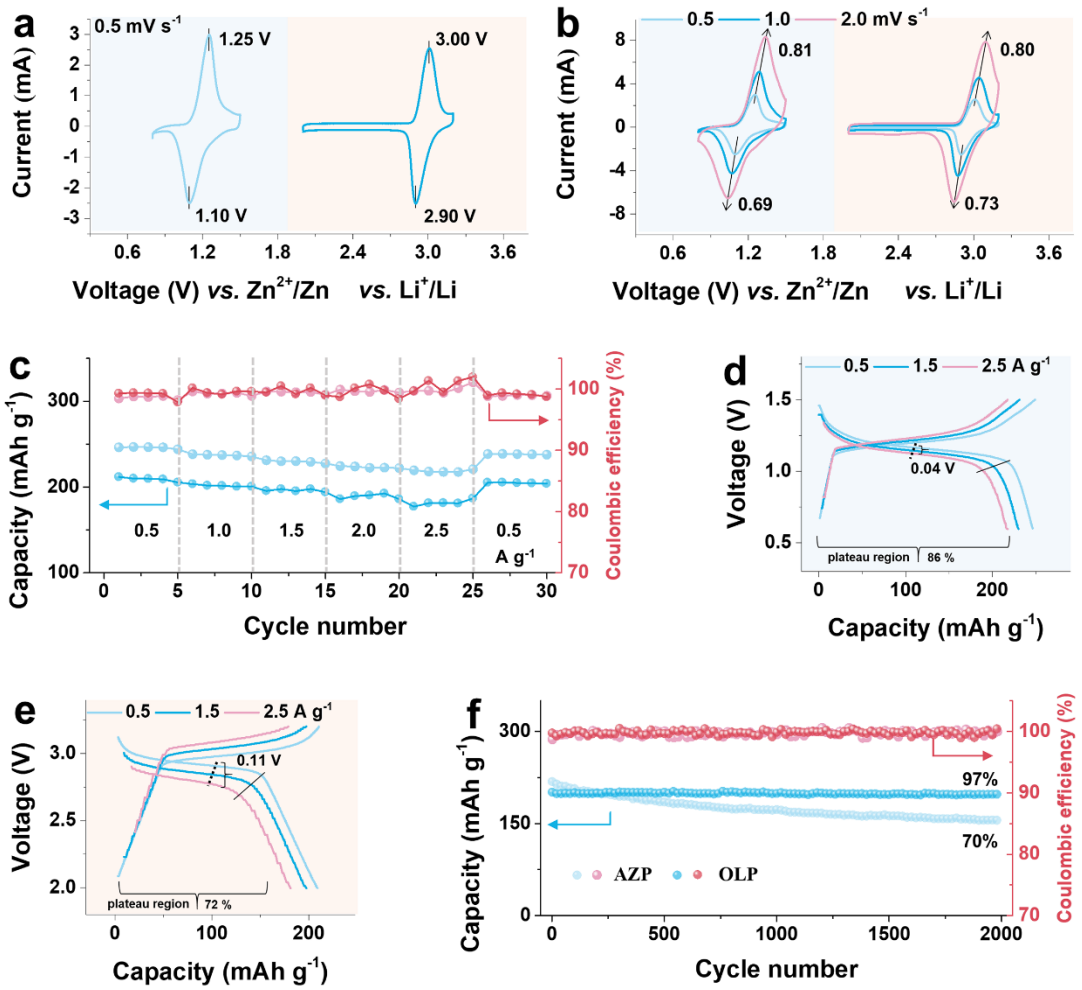

Figure 2. One-electron redox mode in AZP and OLP batteries with PSC based on $ODASnI_4$ microcrystals. a) CV profiles at 0.5 mV s^{-1}. b) CV profiles at 0.5-2.0 mV s^{-1}. c) Rate performance. d) Corresponding GCD curves of the rate performance of the AZP. e) Corresponding GCD curves of the rate performance of the OLP. The black line in GCD curves represents the plateau cutoff mark. f) The prolonged cyclic performances of the two batteries at 1 A g^{-1}.

To examine the redox stability, CV curves of the two batteries were collected at sweep rates of 0.5–2 mV s^{-1}. As illustrated in **Figure 2b**, the redox peaks had similar shapes for all rates without perceptible fluctuations, indicating dynamic electrochemical stability. The absence of any side reactions is also favourable for stability. The current response of both CV curves strengthened as the sweep rates accelerated while the curves remained symmetric. Throughout the scans at different sweep rates, the anodic and cathodic peaks shifted in opposite directions, resulting in the decreased polarisation voltage. Specifically, the polarisation value of the AZP increased from 0.15 to 0.30 V with a fourfold current surge, whereas it increased from 0.10 to 0.25 V for the OLP. Thanks to the rapid redox kinetics, anodic peak hysteresis was as low as 0.09 V for the AZP and 0.10 V for the OLP (**Figure S4**).

The *b* values of the redox peaks were calculated to dissect the reaction kinetics using the following equation: $i = av^b$, where *a* and *b* are variables, *i* signifies the peak current, and *v* signifies the sweep rate.[21] Empirically, for a typical battery regulated by semi-infinite diffusion, *i* and $v^{1/2}$ are linearly related (*i.e.,* $b = 0.5$), whereas, for capacitive electrodes, the linear variables are *i* and *v* (*i.e.,* $b = 1$).[22] As illustrated in **Figure S5**, the *b* values of the cathodic and anodic peaks were determined to be 0.81/0.69 for the AZP and 0.80/0.73 for the OLP, respectively, indicating that the charge storage was controlled by both diffusion and capacitive effects.[23] For conversion-type iodine batteries, a high *b* value is always

considered beneficial because it results in rapid charge carrier diffusion and thus favourable rate capability.

The electrochemical performance was subsequently evaluated in the galvanostatic mode. **Figure 2c** displays the rate performance of the two batteries at 0.5–2.5 A g^{-1}. For the AZP, the discharge capacity reached up to 246 mAh g^{-1}_I at 0.5 A g^{-1}. As the current density increased, the capacity decayed, being 236 mAh g^{-1}_I at 1 A g^{-1}, 229 mAh g^{-1}_I at 1.5 A g^{-1}, and 221 mAh g^{-1}_I at 2.0 A g^{-1} and remaining at 217 mAh g^{-1}_I with 88% retention at 2.5 A g^{-1}. By contrast, for the OLP, the maximum capacity of 210 mAh g^{-1}_I and retention ratio of 86% demonstrated this battery's outstanding reaction kinetics and redox depth. Note that the surplus over the theoretical value may have originated from the cathode additives.[4a] For example, a blank cathode without $ODASnI_4$ delivered a discharge capacity of about 42 mAh g^{-1} at 1 A g^{-1} with typical capacitive features in the same aqueous electrolyte (**Figure S6**). In the corresponding galvanostatic charging-discharging (GCD) curves shown in **Figures 2d** and **2e**, a pair of distinctive plateaus were observed at 1.17/1.20 V versus Zn^{2+}/Zn for the AZP and 2.91/2.97 V versus Li^+/Li for the OLP, respectively. A fivefold increase in current density triggered a median voltage drop of only 0.04 V for the AZP; this value was much smaller than the 0.11 V drop for the OLP, and the difference may have been due to the inherent carrier diffusion advantage of the aqueous electrolyte in the former.[24] The discharge plateau exhibited favourable flatness throughout the whole discharge process, producing stable high-voltage output. The voltage plateau occupation ratios for both batteries were estimated to be more than 72%. During the whole cycle, no observable redox characteristics of Sn^{2+} could be identified. To offer insight into the inert redox activity of Sn^{2+} in the given electrochemical conditions, a pure SnI_2 cathode was prepared and tested in the same aqueous zinc electrolyte. As expected, only redox peaks and plateaus of iodine were detected in its CV and GCD curves, without any signal of Sn^{2+}/Sn^{4+} redox pair (**Figure S7**).

Remarkably, both batteries exhibited excellent cycling stability during room temperature operation, as depicted in **Figure 2f**. At 1 A g^{-1}, the capacity decay of AZP over 2000 cycles

was estimated to be 30%, whereas that of the OLP was almost negligible (~3%). This high stability stands out among all reported iodine-metal batteries.[4b, 25] Furthermore, the reversibility parameter, Coulombic efficiency (CE) value, remained stable at around 100% during the cycling process of both batteries. Under a high mass loading condition of about 3 mg cm^{-2}, the cycle stability of the OLP was still good, and its capacity decay was only 1% in 500 cycles, whereas that of the AZP reached 16% (**Figure S8**). The more severe polyiodide shuttle in the aqueous electrolyte was considered to be the reason for the higher deterioration of AZP's capacity.[17b, 26] The active substances in perovskite cathode suffer an inevitable loss upon cycling.

Multi-electron reactions can effectively boost the energy performance of conversion-type iodine-based batteries. We employed a perovskite-adapted electrolyte by regulating highly electronegative coordinating Cl^- ions to achieve advanced two-electron transfer in AZP and OLP batteries with PSC based on $ODASnI_4$ microcrystals. An electrolyte ($LiCl + ZnSO_4$) was used in AZP (those batteries are abbreviated later on as AZCP), and an electrolyte ($LiCl + LiTFSI + LiNO_3$ in dimethoxyethane/1,3-dioxalane) served as the electrolyte in OLP (those batteries are abbreviated later on as OLCP). CV curves recorded in these two electrolytes at 0.5 mV s^{-1} are displayed in **Figure 3a**. Two pairs of redox peaks are recognizable in both cases, at 1.16/1.23 V and 1.68/1.76 V versus Zn^{2+}/Zn for AZCP and 2.90/3.00 V and 3.40/3.48 V versus Li^+/Li for OLCP; these values are very different from the results achieved in the one-electron redox mode. The two-step reaction pathway may have originated from the two-electron redox conversion, in which low-voltage peaks corresponded to the well-defined I^- redox mode and high-voltage peaks corresponded to the I^+ redox mode. Remarkably, the high-voltage peaks had symmetrical and sharp features with a narrow half-peak width, indicating favourable reversibility and rapid kinetics.[19] Moreover, they delivered stronger current responses than the low-voltage peaks, which may be a consequence of the first electron transfer involving I_3^- formation rather than I_2.[16] In addition,

the two-electron transfer likely drove almost all of the charge transfer involving the PSC, given that the two pairs of redox peaks covered nearly the whole CV curve.[18]

CV curves were obtained using various sweep rates to clarify the long-lasting continuity of the two-electron conversion reaction (**Figure 3b**). For the two types of batteries, a couple of redox peaks with similar shapes were identified in the CV curves obtained at 0.5–2.0 mV s^{-1}. The current response remained symmetric, and the intensities of the high-voltage peaks were always larger than those of the low-voltage peaks. These characteristics indicated the superior thermodynamic stability and high reversibility of the two-electron reactions occurring in these batteries.[4c] For the I^+ redox conversion, the anodic peak shifted to a slightly lower voltage as the sweep rate was increased. The voltage hysteresis of 0.08 V (1.60 V versus 1.68 V) and 0.06 V (3.32 V versus 3.38 V) upon a fourfold scan rate increase was even better than those for I^- (**Figure S9**). Furthermore, the *b* values of the I^+ redox peaks were calculated to shed light on the high-voltage region of the charge storage. As provided in **Figure 3b** and **Figure S10**, AZCP had *b* values of 0.93/0.95, and OLCP had *b* values of 0.77/0.73, showing that the second electron transfer was jointly governed by diffusion and capacitive influences.[23a]

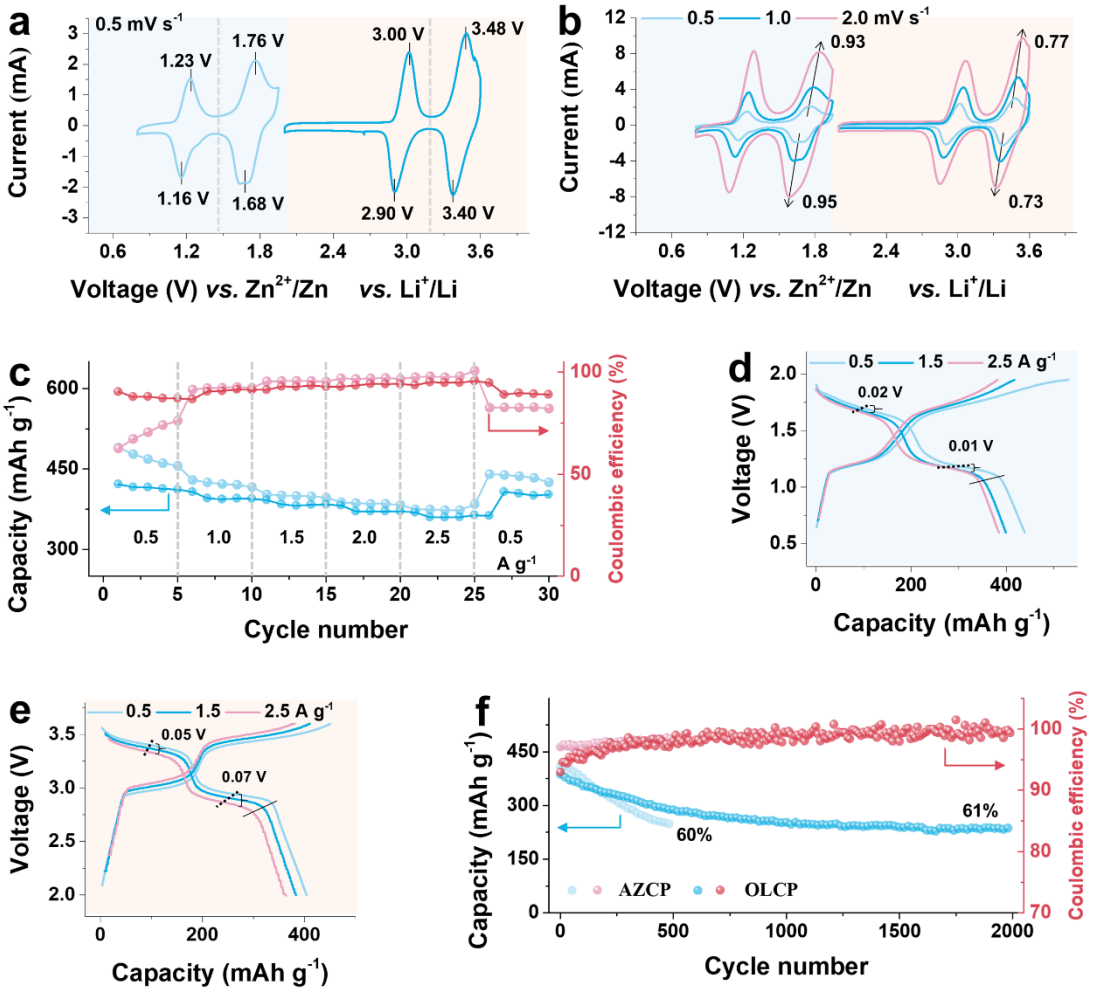

Figure 3. Two-electron redox mode of AZCP and OLCP batteries with PSC based on $ODASnI_4$ microcrystals. a) CV profiles at 0.5 mV s^{-1}. b) CV profiles at 0.5-2.0 mV s^{-1}. c) Rate performance. d) Corresponding GCD curves of the rate performance of the AZCP. e) Corresponding GCD curves of the rate performance of the OLCP. The black lines in GCD curves represent the plateau cutoff mark. f) The prolonged cyclic performance of the two batteries at 1 A g^{-1}.

Subsequently, we investigated the electrochemical performance of AZCP and OLCP batteries based on the two-electron transfer reactions in the galvanostatic mode. First, the rate capability was tested at 0.5–2.5 A g^{-1}, as displayed in **Figure 3c**. With the support of the

two-electron redox chemistry, AZCP offered an extraordinary capacity of 489 mAh g^{-1}_I at 0.5 A g^{-1}, which was almost double that of the one-electron reaction, fluctuating near the theoretical limit of the I^-/I^+ pair.[4a, 8b] This observation verified that the reversible conversion depth of the PSC was complete and echoed the CV results. The discharge capacity was at 423 mAh g^{-1}_I at 1 A g^{-1}, 398 mAh g^{-1}_I at 1.5 A g^{-1}, 384 mAh g^{-1}_I at 2.0 A g^{-1}, and 372 mAh g^{-1}_I at 2.5 A g^{-1}, corresponding to the capacity retention of 87%, 81%, 79%, and 76%, respectively. Thus, advanced redox mechanisms were also revealed for OLCP, which had a maximum capacity of 421 mAh g^{-1}_I and capacity retention of 85%.

The relevant GCD curves are presented in **Figures 3d** and **3e** and contain two pairs of voltage plateaus for both cases—at 1.18/1.20 V and 1.71/1.76 V versus Zn^{2+}/Zn for AZCP and 2.95/3.00 V and 3.41/3.44 V versus Li^+/Li for OLCP, which again confirms the occurrence of two-electron transfer reactions. In the AZCP case, an increase in the current density did not induce considerable hysteresis of the voltage plateau locations, and the deterioration in the capacity was primarily attributable to plateau shortening, confirming excellent reaction kinetics.[17a] More notably, the voltage plateau originating from I^+ redox mode accounted for more than half of the total capacity, in accordance with the CV data. The 1.74 mV/mAh g^{-1}_I plateau decay rate (ratio of voltage drop to specific capacity in the plateau region) was comparable to the 1.21 mV/mAh g^{-1}_I value determined for the first electron transfer, vastly boosting the stable output capability. For OLCP, the I^+ redox plateau was flat, and the decay rate was as low as 1.39 mV/ mAh g^{-1}_I. Despite slightly higher sensitivity to the current density, the midpoint voltage decay of both discharge plateaus remained within 0.07 V. Reasonably, the high voltage plateau coupled with nearly doubled capacity significantly optimized the energy density of the above two batteries.

Figure 3f illustrates the long-term operational performance of AZCP and OLCP batteries at 1 A g^{-1}. AZCP suffered a 40% capacity loss after 500 cycles, which corresponds to 0.08% capacity degradation per cycle. OLCP, by contrast, could achieve stable cycling over 2000 cycles with a much lower decay rate of 0.02% per cycle. This difference may stem

from the different interaction strengths between the redox species and electrolytes, such as the dissolving tendency.[6a, 7] Under an high mass loading of perovskite materials (about 3 mg cm^{-2}), the AZCP and OLCP batteries were still stable in the long-term cycle, delivering a capacity of 399.7 mAh g^{-1}_{I}, and 394.0 mAh g^{-1}_{I} and suffering capacity losses of 42% and 31% in 500 cycles at 1 A g^{-1}, respectively (**Figure S11**).

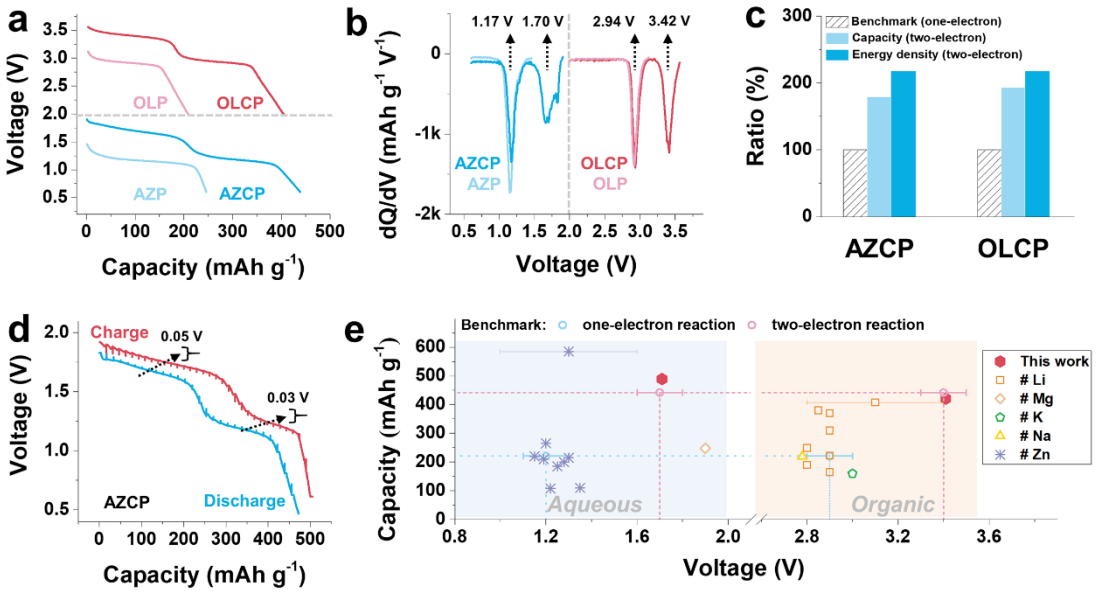

Figure 4. Performance comparison of one-electron and two-electron redox modes of the four batteries (OLP, ACP, OLCP, and AZCP). a) The discharge curves of two redox modes – one-electron and two-electron one. b) Corresponding dQ/dV curves. c) Capacity and energy density enhancement through the two-electron redox mode. d) The GITT curves of the AZCP battery. e) Comparison of the plateau voltage versus capacity between this work and the reported iodine-based batteries (aqueous and organic analogs with different charge carriers) operating under one-electron and two-electron modes.[5b, 25, 29] The error bars represent the theoretical discharge voltage range in different operation conditions.

Our data showed that PSCs based on $ODASnI_4$ microcrystals which were employed in 4 different batteries (OLP, ACP, OLCP, and AZCP) were compatible with well-established

one-electron and leading-edge two-electron redox reactions in both aqueous Zn and organic Li batteries. The discharge curves obtained in these four cases were plotted together to compare their electrochemical properties better. As shown in **Figure 4a**, the regions of the discharge curves driven by the one-electron redox mode for the same electrolyte were similar within the same voltage interval to those for the two-electron redox mode. This agreement meant that the two-electron transfer strictly followed a two-step process.[8b] This is further supported by derived dQ/dV profiles in **Figure 4b**. As expected, the one-electron redox reaction led to a single peak at 1.17 V versus Zn^{2+}/Zn for AZCP and 2.94 V versus Li^{+}/Li for OLCP, whereas the two-electron mode led to two peaks at 1.17 and 1.70 V versus Zn^{2+}/Zn for AZCP and 2.94 and 3.42 V versus Li^{+}/Li for the OLCP. Within the voltage interval of the first electron transfer, the two dQ/dV curves exhibited almost the same shape and peak location, which could be ascribed to their similar plateau regions and voltage inflection points.[27] We noticed the higher intensity of the 1.70 V peak accompanied by a smaller dV compared to the 1.17 V peak, representing a feature of the flat plateau for AZCP. However, the difference in the flatness for OLCP was insubstantial, as evidenced by the two similar peak intensities.

The two-electron redox mechanism significantly boosted the electrochemical performance of the respective batteries. Quantitatively, the capacity and energy density were increased to 179% and 218% for AZCP and 193% and 219% for OLCP, respectively, when the one-electron reaction–based batteries were used as a baseline (**Figure 4c**). Low polarisation is preferred for this kinetic-dominated conversion-type battery. The GCD curve obtained through the galvanostatic intermittent titration technique (GITT) was collected to determine the redox kinetics for AZCP (**Figure 4d**). After the quasi-equilibrium was reached, two sets of plateaus constituted by the low overpotential regions could be observed; they corresponded to the two-electron redox process. The polarisation voltage, which is equal to the difference between the midpoints of charge–discharge plateaus, was estimated to be 0.05 V in the high-voltage plateau region and 0.03 V in the low-voltage plateau region, indicating

that both redox phases were kinetically favourable and that the low-voltage plateau was dominant.[28]

To demonstrate the superiority of the PSC based on $ODASnI_4$ microcrystals serving as electrochemically active cathodes, we compared the performance of the batteries realized in this work to previously reported metal-iodine batteries in terms of the capacity and voltage, considering both aqueous and organic analogs. For reference, the theoretical limitations of one-electron and two-electron chemistry are also plotted. As shown in **Figure 4e**, the electrochemical performance resulting from the two-electron redox reaction in this work (489 mAh g^{-1}_I and 1.71 V for the AZCP; 421 mAh g^{-1}_I and 3.41 V for the OLCP) was superior to well-known counterparts based on I_2 elemental cathodes in one-electron and two-electron transfer models, including aqueous Zn-I_2 and organic Li-I_2, K-I_2, Na-I_2, Mg-I_2 batteries.[5b, 25, 29] Note that such significant improvements in the output voltage and discharge capacity, rather than any tinkering with redox kinetics, may substantially expand the application perspectives of iodine batteries.

Subsequently, we took aqueous Zn-based batteries as a case study to elucidate the two-electron transfer mechanism of the PSC based on $ODASnI_4$ microcrystals by *in-situ* Raman and *ex-situ* XPS characterizations. **Figure 5a** shows the GCD curves, where the selected voltage points were used to collect the corresponding *in-situ* Raman spectra. Those Raman spectra recorded for specific voltage states are provided in **Figure 5b**, where the letters "*c"* and "*d"* before the value in V stand for "*charging*" and "*discharging*", respectively. It is observed that in the stage of the second electron transfer, which began at about 1.6 V, a characteristic Raman peak appeared at around 195-205 cm^{-1} and became more pronounced as the charging progressed, which is a sign of the appearance of $-Cl^-$-I^+ redox species.[4a, 26a] As the discharge proceeded, a weakening Raman peak intensity trend was detected in the following discharge stage. The fully reversible feature in Raman spectra coincided with the generation and reduction of I^+ cations, while Cl^- ions introduced acted as the coordination medium to stabilize the I^+ cations. Note that the Raman peaks at about 100

cm^{-1}, 320 cm^{-1}, and 430 cm^{-1} presented throughout the whole cycle were attributed to the electrochemically inert additives in the electrode and electrolyte.[30] The derived contour pattern in the 140-260 cm^{-1} range presented this variation more clearly. As illustrated in **Figure 5c**, the highlighted area representing the Raman peak intensity emerged near 198 cm^{-1}. It remained symmetric within the voltage interval of *c*1.6 V - *c*1.9 V - *d*1.5 V, which was consistent with the reaction potential of the I^+ redox.

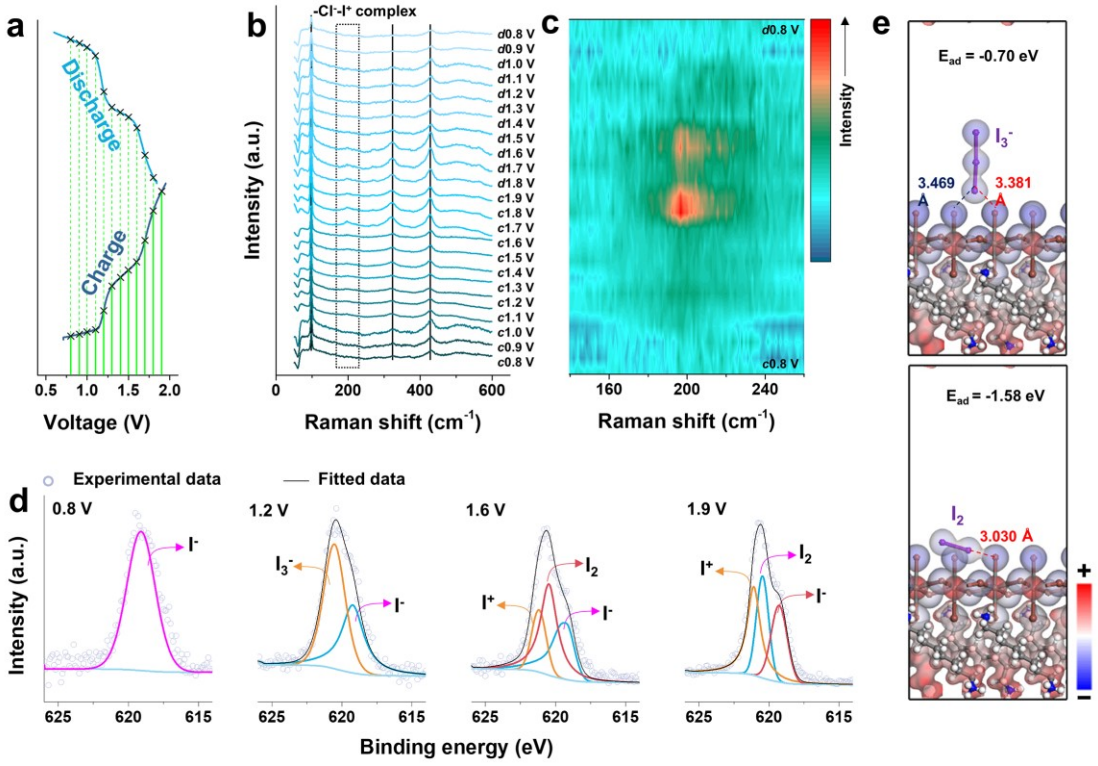

Figure 5. The redox mechanism analysis of the AZCP battery. a) The GCD curve and selected voltage points for *in-situ* characterizations. b) 2D Raman profiles at selected voltage points in the 0-850 cm−1 range. c) The corresponding contour pattern of Raman profiles in the 140-260 cm−1 range. d) I3d XPS spectra at various charge states. e) Visualization of calculated adsorption energy of I_3^- and I_2 at the surface of $ODASnI_4$ perovskite.

In addition, XPS captured the chemical valence shift of iodine in the PSC and the coordination with Cl^- during the charging stage. The high-resolution I3d spectra obtained at various charge states are fitted and plotted in **Figure 5d**. Only a single fitted peak was present in the fully discharged state (0.8 V), located at 619.1 eV and indexed to the I^- ions.[5a] When the cell was charged to 1.2 V to induce the first electron transfer, fitted peaks appeared at 619.2 and 620.5 eV, corresponding to I^- and I_3^- signals, respectively.[4c, 5a, 17a, 26b] I^- was partially oxidized. Advancing to 1.6 V to induce the second electron transfer, the I^+ signal could be recognized at 621.2 eV in addition to the signal of the elemental I_2.[8b, 30] At this stage, the first electron transfer was complete, and I^+ formed with the coordination of Cl^- ions. When the voltage was 1.9 V, the deepened redox behaviour augmented the I^+ signal in the -Cl^--I^+ form. Note that no significant change in the chemical valence of Sn could be identified during cycling. The high-resolution Sn3d XPS spectra in different charging states showed that the binding energy of Sn^{2+} slightly increased at charged (1.5 V) versus discharged (0.8 V) states, probably due to the changed coordination during the redox reactions rather than oxidation to Sn^{4+} cations (**Figure S12**).[13b]

Moreover, the bulging XRD patterns at around 6° indicated that the long-range ordered crystal structure of $ODASnI_4$ perovskite was probably breakdown into short-term orderly amorphous (**Figure S13**). The SEM image confirmed the absence of bulk perovskite microcrystals after the prolonged cycle (**Figure S14**). Further density function theory (DFT) calculation revealed that the short-ordered perovskite lattice and emerging "free" cations/anions at the interface between amorphous and aqueous electrolytes might positively affect electrochemical performance. Specifically, the residual (002) lattice plane of $ODASnI_4$ offered adsorption energy of -0.70 eV and -1.58 eV toward and I_3^- and I_2, respectively, by which halogen bonds are constructed with a length of 3.030 Å for Sn-I…I_2, and of 3.469 or 3.381 Å for Sn-I…I_3^- (**Figure 5e**). In addition, the coordination energy/electrostatic forces between ODA^{2+} and I_3^-, ODA^{2+} and I_2, Sn^{2+} and I_3^-, and Sn^{2+} and I_2 in a vacuum are examined to be -6.21 eV, -1.07 eV, -11.36 eV, and -4.44 eV, respectively, while ignoring the

presence of water molecules (**Figure S15**). The high adsorption energy imposed on I_3^- and I_2 suggested the effectiveness of suppressing the shuttle effect by introducing $ODASnI_4$ perovskite microcrystals into the cathode electrode.[29c]

3. Conclusions

In summary, we demonstrated that an iodine-rich 2D $ODASnI_4$ perovskite is an alternative to conventional elemental I_2, which can be used as a high-performance cathode in organic Li and aqueous Zn batteries. The developed batteries, AZL and OLP, were discovered to work in a well-defined one-electron transfer mode in which distinct discharge plateaus occurred at 1.17 V versus Zn^{2+}/Zn and 2.91 V versus Li^+/Li, respectively. The discharge capacities were approximately 246 mAh g^{-1}_I for both batteries. When the electrolytes were enriched with Cl^- ions for chemical coordination with I^+, two-electron transfer reactions could be triggered for the organic Li and aqueous Zn batteries, delivering considerably higher electrochemical performance. Specifically, high-voltage plateaus (1.71 V versus Zn^{2+}/Zn; 3.41 V versus Li^+/Li) resulted from reversible redox of I^+ cations and almost doubled the discharge capacities (~489 mAh g^{-1}_I for AZCP; 421 mAh g^{-1}_I for OLCP). Furthermore, $ODASnI_4$ exhibited excellent reaction kinetics and decent cycling stability in all demonstrated batteries, indicating a rapid electron transfer mechanism and its effective confinement to iodine. Under the high mass loading condition, the above conversion chemistry remains stable in the prolonged cycle. *In-situ* Raman, *ex-situ* XPS characterizations, and DFT simulation were performed to shed light on the valence shift of iodine. Our research shows the promising potential of metal halide perovskite materials for fabricating aqueous or organic conversion-type metal-iodine batteries. Considering the wide range of perovskite materials that have been developed, our research point out on potential availability of conversion-type batteries with tuneable performance.

Supporting Information

Supporting Information is available from the Wiley Online Library or from the author.

Acknowledgments

This research was supported by the RGC Collaborative Research Fund under Project C1002-21G, Guangdong Province Science and Technology Department (project 2020A0505100014), the Croucher Foundation of Hong Kong, and the Centre for Functional Photonics, City University of Hong Kong. This research was also supported in part by InnoHK Project on [Project 1.4 - Flexible and Stretchable Technologies (FAST) for monitoring of CVD risk factors: Soft Battery and self-powered, flexible medical devices] at Hong Kong Centre for Cerebro-cardiovascular Health Engineering (COCHE).

Author contributions

C.Z. and A.R. conceived the idea and designed the experiments. C.Z., X.L. and S.W. directed the research. S.W. performed the material synthesis, characterization, and electrochemical measurements. D.Z., P.L., Z.C., A.C., Z.H., and G.L. assisted with the electrochemical measurements and data analysis. X.L. S.W., A.R., and C.Z. co-wrote the manuscript. All authors discussed and analyzed the results.

Conflicts of interest

The authors declare no conflicts

Data Availability Statement

The data that support the findings of this study are available from the corresponding author upon reasonable request.

References

[1] a)Y. M. Chiang, *Science* **2010**, 330, 1485; b)Y. Liang, H. Dong, D. Aurbach, Y. Yao, *Nature Energy* **2020**, 5, 646; c)X. Li, *Joule* **2023**, 7, 462.

[2] a)H. Tang, Z. Qu, Y. Yan, W. Zhang, H. Zhang, M. Zhu, O. G. J. M. F. Schmidt, *Materials Futures* **2022**, 1, 022001; b)Y. Liu, J. Cai, J. Zhou, Y. Zang, X. Zheng, Z. Zhu, B. Liu, G. Wang, Y. J. e. Qian, *eScience* **2022**, 2, 389.

[3] a)C. Xia, C. Y. Kwok, L. F. Nazar, *Science* **2018**, 361, 777; b)X. Li, N. Li, Z. Huang, Z. Chen, Y. Zhao, G. Liang, Q. Yang, M. Li, Q. Huang, B. Dong, J. Fan, C. Zhi, *ACS Nano* **2021**, 15, 1718.

[4] a)Y. Zou, T. Liu, Q. Du, Y. Li, H. Yi, X. Zhou, Z. Li, L. Gao, L. Zhang, X. Liang, *Nat Commun* **2021**, 12, 170; b)J. Ma, M. Liu, Y. He, J. Zhang, *Angew Chem Int Ed Engl* **2021**, 60, 12636; c)X. Li, N. Li, Z. Huang, Z. Chen, G. Liang, Q. Yang, M. Li, Y. Zhao, L. Ma, B. Dong, Q. Huang, J. Fan, C. Zhi, *Adv Mater* **2021**, 33, e2006897.

[5] a)H. Pan, B. Li, D. Mei, Z. Nie, Y. Shao, G. Li, X. S. Li, K. S. Han, K. T. Mueller, V. Sprenkle, J. Liu, *ACS Energy Letters* **2017**, 2, 2674; b)H. Tian, T. Gao, X. Li, X. Wang, C. Luo, X. Fan, C. Yang, L. Suo, Z. Ma, W. Han, C. Wang, *Nat Commun* **2017**, 8, 14083.

[6] a)H. Yang, Y. Qiao, Z. Chang, H. Deng, P. He, H. Zhou, *Adv Mater* **2020**, 32, e2004240; b)C. Sun, X. Shi, Y. Zhang, J. Liang, J. Qu, C. Lai, *ACS nano* **2020**, 14, 1176.

[7] F. Wang, Z. Liu, C. Yang, H. Zhong, G. Nam, P. Zhang, R. Dong, Y. Wu, J. Cho, J. Zhang, X. Feng, *Adv Mater* **2020**, 32, e1905361.

[8] a)H. Liu, C. Y. Chen, H. Yang, Y. Wang, L. Zou, Y. S. Wei, J. Jiang, J. Guo, W. Shi, Q. Xu, P. Cheng, *Adv Mater* **2020**, 32, e2004553; b)X. Li, Y. Wang, Z. Chen, P. Li, G. Liang, Z. Huang, Q. Yang, A. Chen, H. Cui, B. Dong, H. He, C. Zhi, *Angew Chem Int Ed Engl* **2022**, 61, e202113576; c)X. Li, Z. Huang, C. E. Shuck, G. Liang, Y. Gogotsi, C. Zhi, *Nat Rev Chem* **2022**, 6, 389.

[9] H. Ge, X. Feng, D. Liu, Y. J. N. R. E. Zhang, *Nano Research Energy* **2023**, 2, e9120039.

[10]a)P. P. Boix, K. Nonomura, N. Mathews, S. G. Mhaisalkar, *Materials today* **2014**, 17, 16; b)S. Wang, S. V. Kershaw, A. L. Rogach, *Chemistry of Materials* **2021**, 33, 5413.

[11]K. Brinkmann, T. Becker, F. Zimmermann, C. Kreusel, T. Gahlmann, M. Theisen, T. Haeger, S. Olthof, C. Tückmantel, M. Günster, *Nature* **2022**, 604, 280.

[12]D. J. Kubicki, S. D. Stranks, C. P. Grey, L. Emsley, *Nat Rev Chem* **2021**, 5, 624.

[13]a)J. W. Lee, S. Tan, S. I. Seok, Y. Yang, N. G. Park, *Science* **2022**, 375, eabj1186; b)S. Wang, Z. Huang, B. Tang, X. Li, X. Zhao, Z. Chen, C. Zhi, A. L. J. A. E. M. Rogach, *Advanced Energy Materials*, 2300922.

[14]S. Chen, C. Wu, B. Han, Z. Liu, Z. Mi, W. Hao, J. Zhao, X. Wang, Q. Zhang, K. Liu, J. Qi, J. Cao, J. Feng, D. Yu, J. Li, P. Gao, *Nat Commun* **2021**, 12, 5516.

[15]S. Wang, J. Popović, S. Burazer, A. Portniagin, F. Liu, K. H. Low, Z. Duan, Y. Li, Y. Xiong, Y. J. A. F. M. Zhu, *Advanced Functional Materials* **2021**, 31, 2102182.

[16]a)C. Bai, F. Cai, L. Wang, S. Guo, X. Liu, Z. Yuan, *Nano Research* **2018**, 11, 3548; b)K. Lu, Z. Hu, J. Ma, H. Ma, L. Dai, J. Zhang, *Nat Commun* **2017**, 8, 527.

[17]a)L. Ma, Y. Ying, S. Chen, Z. Huang, X. Li, H. Huang, C. Zhi, *Angewandte Chemie* **2021**, 133, 3835; b)J. J. Hong, L. Zhu, C. Chen, L. Tang, H. Jiang, B. Jin, T. C. Gallagher, Q. Guo, C. Fang, X. Ji, *Angew Chem Int Ed Engl* **2019**, 58, 15910.

[18]D. Wang, Y. Zhao, G. Liang, F. Mo, H. Li, Z. Huang, X. Li, T. Tang, B. Dong, C. Zhi, *Nano Energy* **2020**, 71, 104583.

[19]C. Yang, J. Chen, X. Ji, T. P. Pollard, X. Lu, C. J. Sun, S. Hou, Q. Liu, C. Liu, T. Qing, Y. Wang, O. Borodin, Y. Ren, K. Xu, C. Wang, *Nature* **2019**, 569, 245.

[20] S. Fleischmann, Y. Zhang, X. Wang, P. T. Cummings, J. Wu, P. Simon, Y. Gogotsi, V. Presser, V. Augustyn, *Nature Energy* **2022**, 7, 222.

[21] G. Liang, X. Li, Y. Wang, S. Yang, Z. Huang, Q. Yang, D. Wang, B. Dong, M. Zhu, C. Zhi, *Nano Research Energy* **2022**, 1, e9120002.

[22] X. Wang, T. S. Mathis, K. Li, Z. Lin, L. Vlcek, T. Torita, N. C. Osti, C. Hatter, P. Urbankowski, A. Sarycheva, M. Tyagi, E. Mamontov, P. Simon, Y. Gogotsi, *Nature Energy* **2019**, 4, 241.

[23] a)Y. Yang, Y. Tang, G. Fang, L. Shan, J. Guo, W. Zhang, C. Wang, L. Wang, J. Zhou, S. Liang, *Energy & Environmental Science* **2018**, 11, 3157; b)X. Li, X. Ma, Y. Hou, Z. Zhang, Y. Lu, Z. Huang, G. Liang, M. Li, Q. Yang, J. Ma, *Joule* **2021**, 5, 2993.

[24] C. Yang, J. Chen, T. Qing, X. Fan, W. Sun, A. von Cresce, M. S. Ding, O. Borodin, J. Vatamanu, M. A. Schroeder, N. Eidson, C. Wang, K. Xu, *Joule* **2017**, 1, 122.

[25] K. Zhang, Z. Jin, *Energy Storage Materials* **2022**, 45, 332.

[26] a)X. Li, M. Li, Z. Huang, G. Liang, Z. Chen, Q. Yang, Q. Huang, C. Zhi, *Energy & Environmental Science* **2018**; b)X. Li, S. Wang, T. Wang, Z. Duan, Z. Huang, G. Liang, J. Fan, C. Yang, A. L. Rogach, C. Zhi, *Nano Energy* **2022**, 98, 107278.

[27] A. Fly, R. Chen, *Journal of Energy Storage* **2020**, 29, 101329.

[28] X. Li, M. Banis, A. Lushington, X. Yang, Q. Sun, Y. Zhao, C. Liu, Q. Li, B. Wang, W. Xiao, C. Wang, M. Li, J. Liang, R. Li, Y. Hu, L. Goncharova, H. Zhang, T. K. Sham, X. Sun, *Nat Commun* **2018**, 9, 4509.

[29] a)P. Li, C. Li, X. Guo, X. Li, C. Zhi, *Bulletin of the Chemical Society of Japan* **2021**, 94, 2036; b)K. Lu, H. Zhang, F. Ye, W. Luo, H. Ma, Y. Huang, *Energy Storage Materials* **2019**, 16, 1; c)P. Li, X. Li, Y. Guo, C. Li, Y. Hou, H. Cui, R. Zhang, Z. Huang, Y. Zhao, Q. J. A. E. M. Li, *Advanced Energy Materials* **2022**, 12, 2103648; d)C. Bai, H. Jin, Z. Gong, X. Liu, Z.

Yuan, *Energy Storage Materials* **2020**, 28, 247; e)Q. Zhao, Y. Lu, Z. Zhu, Z. Tao, J. Chen, *Nano Lett* **2015**, 15, 5982.

[30]Q. Guo, K.-I. Kim, S. Li, A. M. Scida, P. Yu, S. K. Sandstrom, L. Zhang, S. Sun, H. Jiang, Q. Ni, *ACS Energy Letters* **2021**, 6, 459.

TOC

The iodine-rich two-dimensional perovskite materials work as an innovative iodine cathode for high-performance iodine-based batteries, which are well suited to diversified electrolytes and two-electron redox modes, delivering large capacity, high output voltage, and high energy density.